Earth and Planetary Science Letters 301 (2011) 297–306

Contents lists available at ScienceDirect

Earth and Planetary Science Letters

journal homepage: www.elsevier.com/locate/epsl

Geomagnetic field intensity: How high can it get? How fast can it change? Constraints from Iron Age copper slag

Ron Shaar [a,*], Erez Ben-Yosef [b], Hagai Ron [a], Lisa Tauxe [c], Amotz Agnon [a], Ronit Kessel [a]

[a] The Institute of Earth Sciences, The Hebrew University of Jerusalem, Givat Ram, Jerusalem, 91904, Israel
[b] Department of Anthropology, University of California, San Diego, La Jolla, CA, 92093, USA
[c] Scripps Institution of Oceanography, University of California, San Diego, La Jolla, CA, 92093, USA

ARTICLE INFO

Article history:
Received 27 July 2010
Received in revised form 24 October 2010
Accepted 7 November 2010
Available online 8 December 2010

Editor: P. DeMenocal

Keywords:
archaeomagnetism
paleomagnetism
paleointensity
secular variations
Iron Age
slag
Timna
archaeometallurgy
radiocarbon
^{14}C
Thellier

ABSTRACT

The intensity of the geomagnetic field varies over different time scales. Yet, constraints on the maximum intensity of the field as well as for its maximum rate of change are inadequate due to poor temporal resolution and large uncertainties in the geomagnetic record. The purpose of this study is to place firm limits on these fundamental properties by constructing a high-resolution archaeointensity record of the Levant from the 11th century to the early 9th century BCE, a period over which the geomagnetic field reached its maximum intensity in Eurasia over the past 50,000 years. We investigate a ^{14}C-dated sequence of ten layers of slag material, which accumulated within an ancient industrial waste mound of an Iron Age copper-smelting site in southern Israel. Depositional stratigraphy constrains relative ages of samples analyzed for paleointensity, and ^{14}C dates from different horizons of the mound constrain the age of the whole sequence. The analysis yielded 35 paleointenisty data points with accuracy better than 94% and precision better than 6%, covering a period of less than 350 years, most probably 200 years. We construct a new high-resolution quasi-continuous archaeointensity curve of the Levant that displays two dramatic spikes in geomagnetic intensity, each corresponding to virtual axial dipole moment (VADM) in excess of 200 ZAm^2. The geomagnetic spikes rise and fall over a period of less than 30 years and are associated with VADM fluctuations of at least 70 ZAm^2. Thus, the Levantine archaeomagnetic record places new constraints on maximum geomagnetic intensity as well as for its rate of change. Yet, it is not clear whether the geomagnetic spikes are local non-dipolar features or a geomagnetic dipolar phenomenon.

1. Introduction

The intensity of Earth's magnetic field changes in a complicated fashion on timescales ranging from days to millions of years. In an effort to characterize field behavior and to understand the geodynamo, high-quality paleointensity data describing the evolution of the field with time are required. The maximum value of the field as well as its rate of change are two fundamental characteristics, and basic questions one might ask in paleointensity research are: "How fast can field intensity change?" and "How strong can the field get?"

The maximum value and rate of change of past geomagnetic field can be assessed using global stacks of paleointensity data (e.g. Knudsen et al., 2008; Yang et al., 2000), local stacks (e.g. Genevey et al., 2008), and paleosecular geomagnetic models (Korte and Constable, 2003, 2005a; Korte et al., 2009). Global stacks, local archaeointensity stacks, and spherical harmonics models go as far as 50, 10, and 7 ka, respectively. These suggest maximum field intensities, in terms of virtual axial dipole moment (VADM), of 120–150 ZAm^2. High-resolution models of the recent past [i.e. GUFM covering the past 400 years, Jackson et al. (2000), and International Geomagnetic Reference Field covering the past 50 years] suggest a maximum rate of change for local field intensity of 25 ZAm^2 per 100 years. However, recent evidences from archaeological sources (archaeomagnetism) suggest a presence of high frequency features, with wavelengths of the order of tens of years. These suggest that models and stacks might smooth high frequency features out. Examples are: "archaeomagnetic jerks" (Gallet et al., 2003), which are abrupt changes in the direction and the intensity of the field, and "geomagnetic spikes" (Ben-Yosef et al., 2009), which are short episodes of exceptionally high field intensity in excess of 200 ZAm^2. Yet, a fundamental problem with studying such short-lived features is that a proper description of short periods requires time-resolution and accuracy, which are beyond the capability of most conventional sampling techniques (mostly based on lava flows and archaeological baked-clay artifacts, e.g. Donadini et al., 2007; Tauxe and Yamazaki, 2007; Valet, 2003).

Copper slag material, a metallurgic waste of an ancient copper-smelting technology, was recently introduced as a new and useful paleomagnetic recorder (Ben-Yosef et al., 2008a,b; Ben-Yosef et al.,

* Corresponding author. Tel.: +972 2 6586856; fax: +972 2 5662581.
E-mail address: ron.shaar@mail.huji.ac.il (R. Shaar).

0012-821X/$ – see front matter © 2010 Elsevier B.V. All rights reserved.
doi:10.1016/j.epsl.2010.11.013

2009; Shaar et al., 2010). Copper slag was produced when the metallic copper accumulated in the bottom of the smelting furnace, and the residual melt solidified as black chunks in the upper part of the furnace or as solid plates in front of the smelting installation (by deliberate tapping of the residual melt). This industrial waste accumulated sometimes in debris mounds at the production site, at a rate of up to two meters per century (Levy et al., 2008). Ben-Yosef et al. (2009) studied an Iron Age waste mound of slag in southern Jordan and employed a relative stratigraphy technique that yielded a temporal archaeointensity resolution for the samples of decades. Thus, slag material provides a unique opportunity to circumvent difficulties in paleointensity studies of short-term geomagnetic features. Shaar et al. (2010) tested the suitability of slag for absolute paleointenisty experiments and quantified the accuracy of paleointensity estimates obtained from slag material. Using laboratory-produced single-domain-like slag they showed that carefully controlled paleointensity experiments on suitable slag material yield accuracy of better than 94% and precision of better than 5%.

This study follows Ben-Yosef et al. (2009) who discovered the existence of two geomagnetic spikes during the Iron Age in an archaeointensity study of a slag mound in southern Jordan. The Levantine spikes were associated with a relatively strong geomagnetic dipole (Korte and Constable, 2005b), a peak in the Eurasian archaeointensity stack of the past 8 ky (Genevey et al., 2008), and a peak in the global paleointensity stack of the past 50 ky (Knudsen et al., 2008). Figure 1a illustrates the timing of the geomagnetic spikes with respect to global paleointensity models and compilations, and Figure 1b shows previous archaeointenisty data from the Near East. As seen in Figure 1a the spikes represent the climax of a rapidly growing field and, therefore, their values can constrain the maximum intensity that the geomagnetic field can reach. In addition, the duration of the spikes can constrain the maximum rate of change of the field.

In this study, we aim to provide a highly detailed archaeointenisty curve of the Levant during the spike episodes, and further constrain the duration and the maximum value of the Levantine spikes, as well as the variations that accompany them. Here we apply the archaeomagnetic sampling technique established in Ben-Yosef et al. (2009) and the paleointensity procedure established in Shaar et al. (2010) in order to reach maximum temporal resolution of less than decades and paleointensity accuracy of better than 94%.

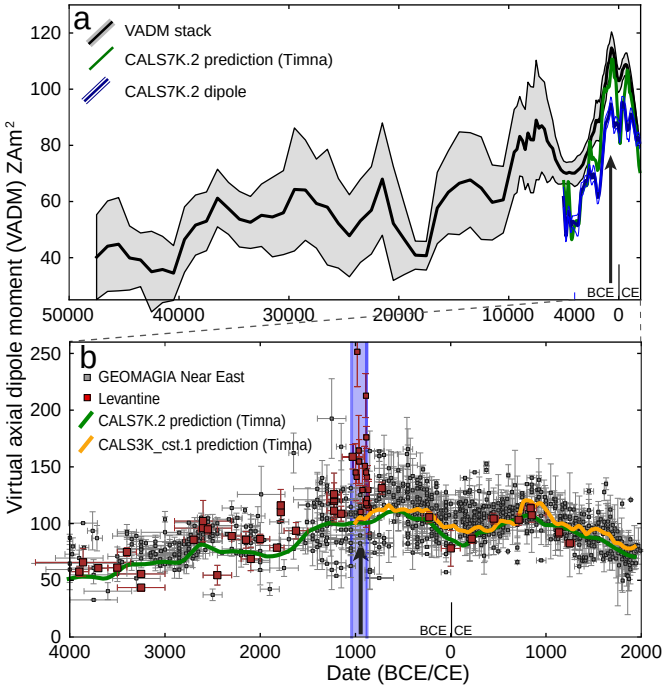

Fig. 1. Summary of previous studies. a) Gray line: average global VADM and the associated error estimates (2σ) obtained by stacking paleointensity data of the past 50 ky (Knudsen et al., 2008). Blue line is the dipole moment calculated by CALS7K.2 model (Korte and Constable, 2005a,b). Green line is the prediction of CALS7K.2 model (Korte and Constable, 2005a) for the location of Timna-30. Arrow marks the peak at ~3 ka. b) VADMs of the Near East obtained by filtering the GEOMAGIA database (Korhonen et al., 2008) according to age (past 6000 years), location (latitude between 20°N to 50°N, longitude between 10°E to 50°E), method (Thellier family), and standard deviation (<15%). Levantine data, including the geomagnetic spikes (Ben-Yosef et al., 2009), are colored in red. Location of the sites is shown in Fig. 2a. Green (orange) line is the prediction of CALS7K.2 model (Korte and Constable, 2005a) [CALS3K_cst.1 model (Korte et al., 2009)] for the location of Timna-30. The blue area and the arrow mark the spikes episode studied here.

2. Methods

2.1. Archaeomagnetic sampling and radiocarbon dating

Slag samples were collected from site Timna-30 (Fig. 2), located in the Arava valley, southern Israel, near the ancient copper mines of Timna. Following the excavation of Rothenberg (1980), we re-excavated an exposed slag mound, 1.5-meters in height that had some indications of being partially contemporaneous with the archaeomagnetic spikes recorded at Khibat en Najas (KEN, Ben-Yosef et al., 2009). The excavation followed Shaar et al. (2010) who sampled slag from this mound in order to test suitability for paleointensity study and to study the magnetic properties responsible for the optimal behavior in paleointensity experiments. We designed the excavation especially to sample the most suitable slag for paleointensity in its most clear archaeological and stratigraphic context.

The excavation revealed ten layers containing two different types of slag in the mound (Fig. 3). Type-A slag (Mn-rich slag, Shaar et al., 2010) is found in the uppermost layer (layer 0 in Fig. 3) and type-B slag (Fe-rich slag, Shaar et al., 2010) in the lowermost layers (layers 1–9 in Fig. 3). The relative stratigraphy and the chronology of the layers are given in Section 3.1. We exposed a cross-section that revealed a clear depositional stratigraphy from top to bottom, and established a 50×30 cm grid over it. We sampled over 100 pieces of slag of both types, as well as two high-temperature baked-clay samples and three pottery samples. In addition, we took over 50 short-lived organic samples from 16 different locations in the cross-section. The precise location of each sample was carefully measured with respect to the grid, and documented on a scaled sketch at a resolution of 1 cm.

The slag mound was dated using five short-lived samples (seeds, a wood bark and a twig) collected from five different horizons in the section. Radiocarbon was analyzed for dating at the NSF AMS laboratory at the University of Arizona. We used the Oxcal4.1.6 program (Ramsey, 2009; Reimer et al., 2009) for calibrating the ^{14}C ages as well as for Bayesian analysis. The Bayesian age modeling of the mound follows the methodology described in Levy et al. (2008).

2.2. Absolute paleointensity experiments

A total of fifty-two slag samples, as well as one pottery sample, and one tuyère sample (high-temperature baked-clay nozzle of the bellow pipes) were analyzed for absolute paleointensity. The samples were measured at the paleomagnetic laboratories of the Institute of Earth Sciences, the Hebrew University of Jerusalem, and Scripps Institution of Oceanography, University of California, San Diego. At least three specimens per sample were prepared by isolating small chips, 1 to 5 mm in size, from the glassy outer margin of each slag sample. The chips were wrapped in glass microfiber filters and glued inside 12-mm diameter glass vials using potassium-silicate glue (KASIL). NRM was measured as a selecting criterion, rejecting specimens with NRM$<10^{-7}$ Am^2.

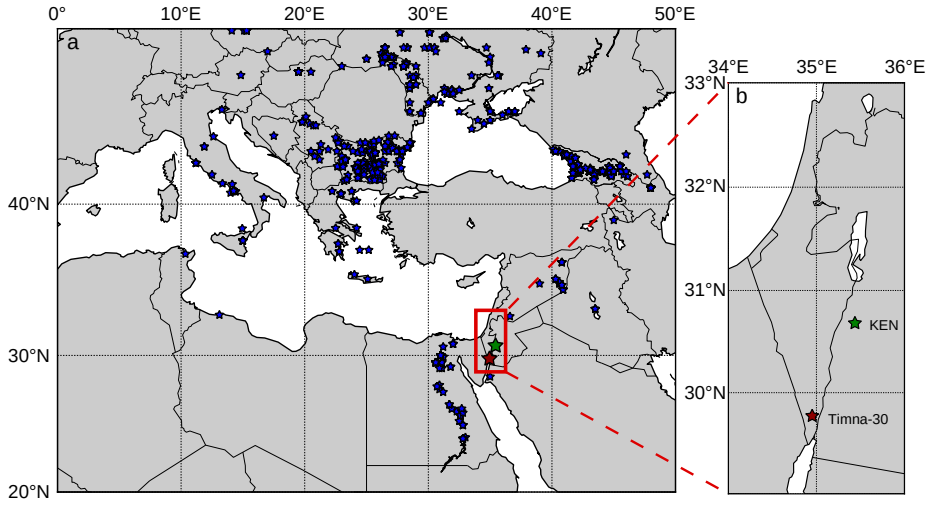

Fig. 2. a) Map of Near East area showing the location of the sites displayed in Fig. 1. b) Location map of Khirbat en-Nahas (KEN, latitude 30.681°N, longitude 35.437°E), and Timna-30 (latitude 29.77°N, longitude 34.95°E).

The absolute paleointensity experiments followed the IZZI protocol of Tauxe (2010) and Tauxe and Staudigel (2004), using an oven field of 75 μT or 80 μT (as close as possible to the expected field intensity). Reproducibility of partial thermal remanence acquisition was routinely checked (pTRM checks) every second temperature step. Paleointensity estimates were corrected for anisotropy using anisotropy tensor, calculated through the acquisition of TRM or ARM in six positions (x, -x, y, -y, z, -z) in the specimen's coordinate system. A comparison of TRMs acquired at inverted positions (i.e. +x and −x+y and −y and+z and −z) was used to monitor the anisotropy of TRM (ATRM) procedure. Specimens with a difference larger than 6% were rejected. Non-linear TRM (NLT) behavior (Selkin et al., 2007; Shaar et al., 2010) was checked whenever the difference between the calculated ancient field and the oven's field exceeded 10 μT for type-A slag. Alterations of the magnetic properties during the ATRM and NLT procedures were monitored by additional TRM acquisition tests at the end of each procedure. The paleointensity estimates were compensated for the effect of different cooling rates for the pottery specimens following the procedure described in Genevey and Gallet (2002), using a slow cooling rate of 10 h, and fast cooling rate of half an hour at a temperature of 600 °C, assuming an ancient cooling rate of 24 h. The final calculations were accepted or rejected according to a set of accepting criteria parameters, with threshold values listed in Section 2.3.

2.3. Paleointensity data reduction

A fundamental, yet still hotly debated, issue in paleointensity research is how to best define acceptance criteria for the results of the

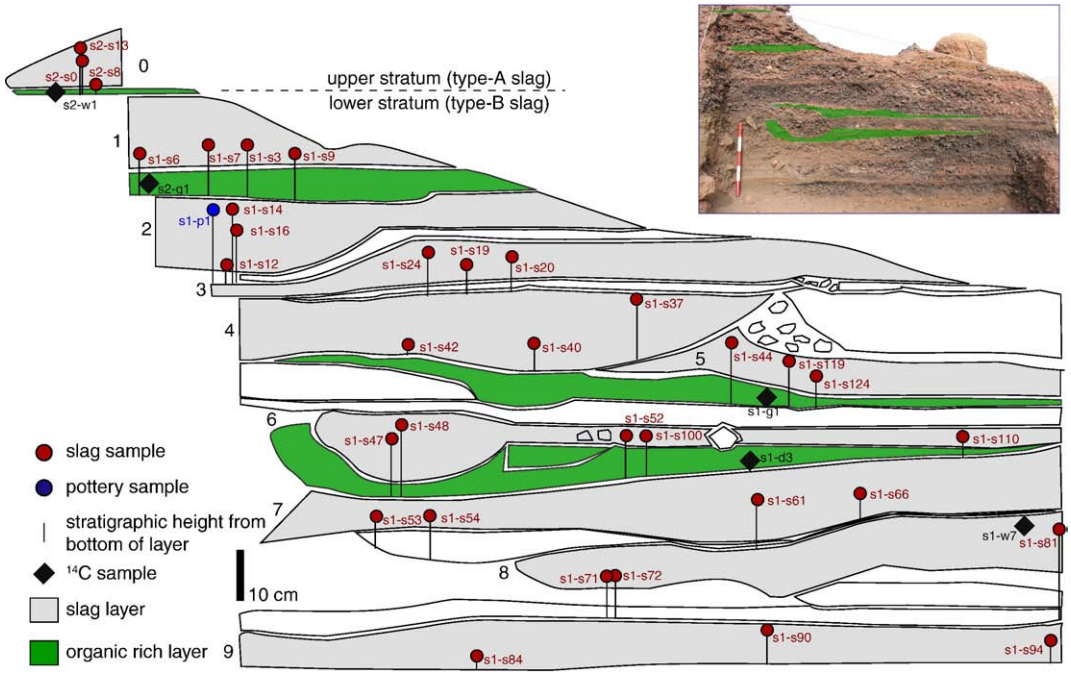

Fig. 3. A scaled sketch of the slag debris cross-section in site Timna-30. Photo of the section is in the inset.

Thellier paleointensity experiments (e.g. Ben-Yosef et al., 2008a; Biggin and Thomas, 2003; Selkin and Tauxe, 2000; Tauxe, 2010; Tauxe and Yamazaki, 2007). In this study we follow Shaar et al. (2010) who calculated cutoff values of paleointensity statistics from a set of laboratory-produced samples that were used for testing the paleointensity methodology. Here we define cutoff values for these paleointensity statistics parameters, and apply them as acceptance criteria. The cutoff values are listed in Table 1, and they were chosen to be as close as possible to the values obtained from the laboratory-produced slag. The cutoff values are strict with respect to similar published paleointenisty studies, and they allow us to accept only specimens that display a stable NRM (MAD<6°, Kirschvink, 1980) with highly linear Arai plots (β<0.05, Coe et al., 1978; Selkin and Tauxe, 2000) over segments of at least 80% of a uni-vectorial paleomagnetic vector (Fvds>0.8, Tauxe, 2010; DANG<6°, Tauxe and Staudigel, 2004). Sample means were calculated using at least three successful specimens. Samples with standard deviations higher than 6% were rejected. In cases where at least 5 specimens passed the selecting criteria, but the standard deviation was higher than 6% due to one anomalous specimen, we ignored the anomalous specimen in the final calculation.

3. Results

3.1. Archaeological stratigraphy

Figure 3 shows a scaled cross-section drawing of Timna-30 slag mound. The cross-section reveals 10 distinct layers of slag debris (colored in gray), as well as 3 soil layers rich in organic material (colored in green). The field relations demonstrate a clear depositional sequence of the layers. The uppermost layer (layer 0) is composed of type-A slag, and the other nine layers (layers 1–9) are composed of slag type-B (see Shaar et al., 2010 for details). The locations of slag samples that successfully passed the paleointensity experiments (see Section 3.2), as well as the locations of ^{14}C samples are displayed on the scaled sketch.

In order to describe the stratigraphic as well as chronologic relations between samples within the section, we assigned a stratigraphic height for each sample using the following procedure: we first measured the maximum thickness of each layer, and calculated a composite stratigraphic height of the whole mound using the sum of all thicknesses. Then, a stratigraphic height of each sample was calculated by the cumulative stratigraphic height of the bottom of the layer plus the height of the sample within the layer (shown as a vertical short line in Fig. 3).

3.2. Absolute paleointensity results

Figure 4 shows representative behavior of the slag material in the paleointensity experiments, displayed as Arai plots (Nagata et al., 1963). Figure 4a shows the typical behavior of type-A slag,

Table 1
Cutoff values of quality criteria.

	Specimen[a]					Sample[b]	
	β	f_{vds}	MAD	DANG	DRATS	N_{min}	σ (%)
Archaeological slag (this study)	0.055	0.8	6	6	10	3	6
Re-melted slag (Shaar et al., 2010)	0.04	0.6	8	4	14	–	–

[a] β — scatter parameter (Coe et al., 1978; Selkin and Tauxe, 2000); f_{VDS} — fraction of the total remanence (Tauxe and Staudigel, 2004); MAD — maximum angle of deviation (Kirschvink, 1980); DANG — deviation of the ANGle (Tauxe and Staudigel, 2004); DRATS — difference RATio sum (Tauxe and Staudigel, 2004). See also Tauxe (2010).
[b] N_{min} — number of specimens per sample; σ (%) — standard deviation around the sample mean.

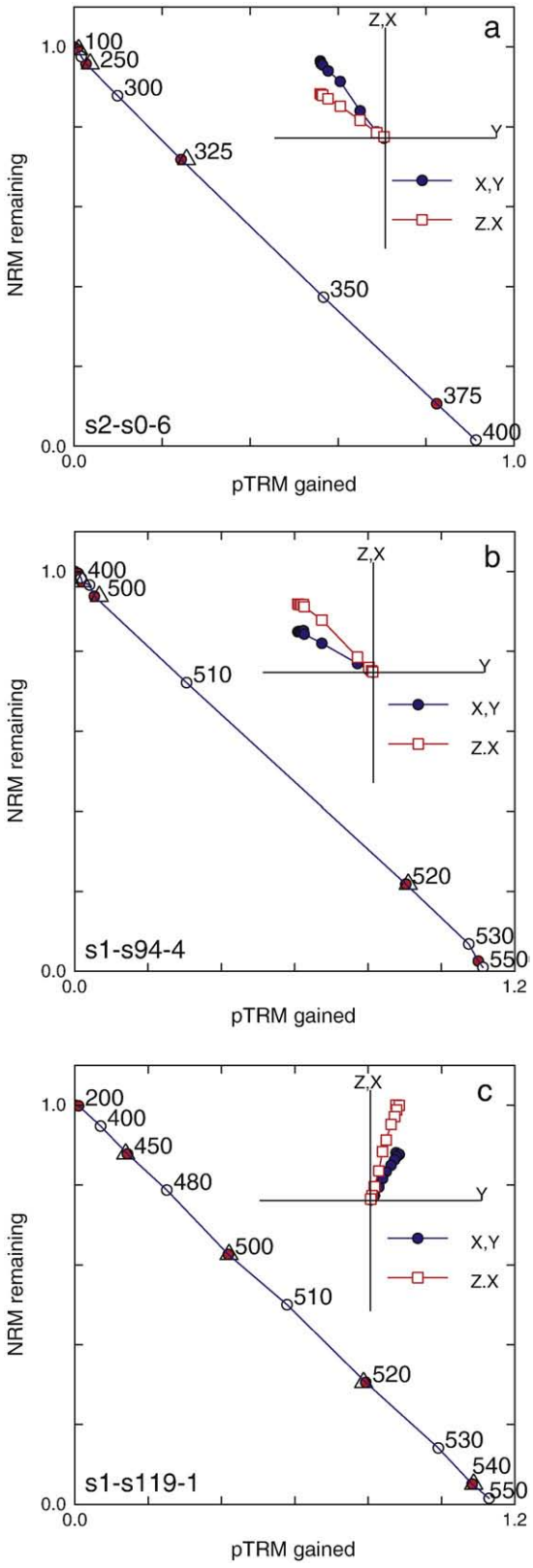

Fig. 4. Selected Arai plots demonstrating the high-quality of the slag samples. Open (closed) circles are the Infield–Zerofield (Zerofield–Infield) steps of the IZZI experiments (see Tauxe, 2010 for details). pTRM checks, performed every second temperature step are shown as triangles. All plots are highly linear. Orthogonal projections of the zerofield steps, showing convergence toward the origin, are shown in the insets. Red squares (blue circles) are projections on the XZ plane (YZ plane) in the specimen coordinates.

demonstrating blocking temperatures below 400 °C (NRM carrier is jacobsite, Shaar et al., 2010), and Figure 4b shows a typical behavior of type-B slag, demonstrating blocking temperatures between 500 °C and 550 °C (NRM carrier is non-stoichiometric magnetite, Shaar et al., 2010). Figure 4c shows a behavior that cannot be classified as type-A or type-B according to blocking temperature spectrum, demonstrating an interval of 400 °C to 550 °C. Such samples resemble the appearance of type-B, and in this study we assign this behavior as type-B slag.

The final paleointensity calculations of a total of 35 samples (3 of type-A slag, 31 of type-B slag, and 1 pottery) that passed the selection criteria (Table 1) are given in Table 2. Figure 5b displays the paleointensity results according to the stratigraphic height of the samples, whereas horizontal error-bars represent the boundaries of the layers in which the samples were found and vertical error-bars represent the standard deviation of the samples means. The results demonstrate excellent grouping of paleointensity estimates within closely spaced stratigraphic heights, with exceptionally high values observed in layers 0 and 5–6. The behavior at site KEN (Fig. 2, Ben-Yosef et al., 2009), which is of the same age as site Timna-30 is given in Figure 5a. Both datasets show similar behavior of double-peak geomagnetic spikes (colored in pale blue). We therefore correlate the Timna-30 spikes to the Jordanian geomagnetic spikes as the most parsimonious interpretation, and provide a correlation between the two datasets in Section 3.4.

The entire dataset as well as our interpretations are available in the MagIC database (http://earthref.org). The paleointenisty statistics of the results are available in the supplementary data associated with the online version of the article.

3.3. Radiocarbon dates and chronological constraints

Although charcoals appear in large quantity in the section we preferred not to use them for dating in order to avoid an "old wood effect" that might bias the results towards earlier dates, but instead used short-lived material. Seeds, such as dates, grapes, wheat and olives, are optimal samples, representing a human waste originating in the food of the workers in the site. It is reasonable to assume that the time elapsed from harvesting of a fruit, eating, and throwing it to the waste mound is very short. Therefore, the seeds (samples s2-g1, s1-g1, and s1-d3 in Fig. 3) best represent the age of the layer in which they were found. Since seeds were not found in the uppermost and lowermost layers, we used a thin unburned wood bark (sample s1-w7) and a twig, 2-mm in thickness (sample s2-w1), for dating of the lower and the upper layer, respectively.

Table 3 lists the ^{14}C ages of the organic samples in Timna-30. Table S1, supplementary material, lists the Bayesian modeled ages, assuming stratigraphic order of the samples, and Figure S1, supplementary material, plots the distribution functions of the Bayesian modeled ages. The 95% confidence interval (2σ) and the 67%

Table 2
Summary of archaeointensity results from site Timna-30 (latitude 29.771, longitude 34.948).

Layer[a]	Sample	Stratigraphic height (cm)[b]	Modeled age (BCE)[c]	B (μT)[d]	VADM (ZAm^2)	Number of specimens
0	s2-s0	153	894 (895–890)	81.4 ± 1.9	159 ± 4	5
0	s2-s7	155	892 (895–890)	81.5 ± 4.7	159 ± 9	3
0	s2-s8[e]	157.5	890 (895–890)	104.2 ± 6.3	204 ± 12	4
1	s1-s3	139.5	907 (895–890)	69.1 ± 1.8	135 ± 4	4
1	s1-s6	138.5	908 (913–895)	72.2 ± 3.1	141 ± 6	5
1	s1-s7	139.5	907 (913–895)	72.4 ± 0.9	142 ± 2	4
1	s1-s9	136.5	910 (913–895)	64.7 ± 1.9	127 ± 4	3
2	s1-s12	118.5	926 (913–895)	70.6 ± 0.6	138 ± 1	5
2	s1-s14	128	918 (930–913)	65.8 ± 3.4	129 ± 7	8
2	s1-s16	126.5	919 (930–913)	71.0 ± 1.9	139 ± 4	5
2	s1-p1[f]	127.5	918 (930–913)	73.9 ± 1.9	145 ± 4	3
3	s1-s19	112.5	932 (939–930)	68.8 ± 3.2	135 ± 6	3
3	s1-s20	111.5	933 (939–930)	76.3 ± 3.3	149 ± 6	4
3	s1-s24	113.5	931 (939–930)	76.1 ± 3.0	149 ± 6	5
4	s1-s37	101.5	942 (955–939)	71.2 ± 4.0	139 ± 8	5
4	s1-s40	93.5	950 (955–939)	71.3 ± 1.1	139 ± 2	3
4	s1-s42	90.5	953 (955–939)	78.4 ± 3.3	153 ± 6	3
5	s1-s44	84	959 (971–955)	83.6 ± 3.7	164 ± 7	5
5	s1-s119	79.5	963 (971–955)	70.2 ± 4.0	137 ± 8	4
5	s1-s124	79	963 (971–955)	73.4 ± 1.7	144 ± 3	4
6	s1-s52	60	981 (971–955)	96.8 ± 1.4	189 ± 3	4
6	s1-s100	60	981 (971–955)	90.4 ± 5.2	177 ± 10	4
6	s1-s110	54.5	986 (990–971)	73.4 ± 2.6	144 ± 5	4
6	s1-s47[e]	63	978 (990–971)	71.7 ± 2.7	140 ± 5	6
6	s1-s48	66	975 (990–971)	67.7 ± 3.7	133 ± 7	4
7	s1-s61	42.5	997 (990–971)	76.8 ± 3.9	150 ± 8	5
7	s1-s66[e]	38.5	1001 (1007–990)	77.3 ± 2.8	151 ± 6	4
7	s1-s53	35	1004 (1007–990)	72.2 ± 2.0	141 ± 4	5
7	s1-s54	35	1004 (1007–990)	71.1 ± 2.4	139 ± 5	3
8	s1-s71	18	1020 (1028–1007)	72.4 ± 3.9	142 ± 8	4
8	s1-s72	18	1020 (1028–1007)	67.2 ± 1.6	132 ± 3	4
8	s1-s81	28	1011 (1028–1007)	69.8 ± 2.2	136 ± 4	4
9	s1-s84	3.5	1034 (1037–1028)	79.9 ± 3.9	156 ± 8	6
9	s1-s90	7	1030 (1037–1028)	74.3 ± 1.0	145 ± 2	4
9	s1-s94	5	1032 (1037–1028)	72.2 ± 2.8	141 ± 6	4

[a] Layer numbering is as Fig. 3.
[b] See Section 3.1 for details.
[c] Modeled age according to age model illustrated in Fig. 6. Ages in brackets are modeled ages for the boundary of the layer.
[d] Confidence bounds on sample averages were determined by the standard deviation around the sample mean.
[e] One specimen was rejected due to anomalous value (see Section 2.3 for details).
[f] Pottery sample (all other samples are slag).

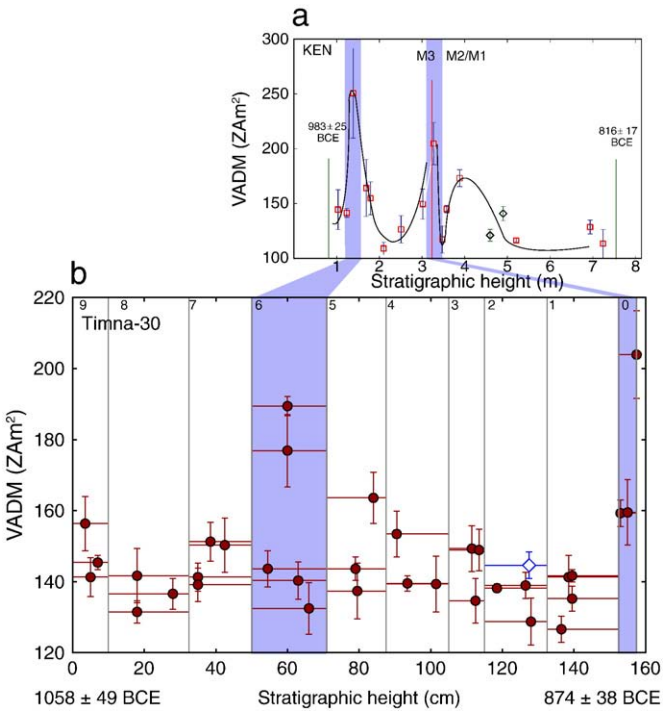

Fig. 5. VADM versus height curves. a) KEN dataset (Ben-Yosef et al., 2009). b) Timna-30 (this study). Vertical lines show heights of the layer boundaries, red circles are slag samples, blue diamond is a pottery sample, vertical error-bars are the standard deviation around the sample's mean, horizontal error-bars represent the boundary of the layer. The layers are numbered according to Fig. 3. The geomagnetic spikes in both records are highlighted in pale blue. Ages at the boundaries of each dataset represent the 1σ confidence-boundaries of each of the sections, inferred from Bayesian models of each site.

confidence interval (1σ) of the whole cross-section, inferred from the Bayesian analysis, are 1109–836 BCE, and 1129–804 BCE, respectively. The ^{14}C analysis indicates, therefore, that the age range of the Timna-30 mound overlaps with that of the KEN section analyzed in Ben-Yosef et al. (2009) and Levy et al. (2008).

3.4. A composite age–height model

Figure 5 shows the archaeointensity results from this study as well as the published data of Ben-Yosef et al. (2009) from the site of Khirbat en-Nahas (KEN) in Jordan (Fig. 2). The two datasets together demonstrate a behavior of two short-lived double-peak geomagnetic spikes. To further constrain the chronology of this behavior we correlate the two datasets to construct a composite age model using a Bayesian analysis of the ^{14}C ages. The assumptions of the Bayesian model, illustrated in Figure S3 in the supplementary material, are as follows: 1) the early geomagnetic spike in KEN is of the same age as the spike found in layer 6 in Timna-30; 2) the late geomagnetic spike in KEN (M3–M2/M1 boundary) is of the same age as the spike in layer 0 in Timna-30; 3) the stratigraphic order of KEN ^{14}C samples is as listed in Ben-Yosef et al. (2009) and Levy et al. (2008); and 4) the stratigraphic order of Timna-30 ^{14}C samples is as illustrated in Figure 3.

The KEN dataset was split in this study into two sections: an eastern wall section and a western wall section [see Fig. 4 in Ben-Yosef et al. (2009)], in order to enhance the robustness of the model and obtain a better resolution. We used a total of 13 ^{14}C samples from both sites for the model, rejecting two samples that showed anomalously old ages. Sample #17637 resulted in low value of parameter A in the Oxcal program, and was indicated before as probably biased by an old wood effect (Levy et al., 2008), and sample #17647 reduces drastically the overall value of A parameter. The resulting statistics of the combined Bayesian age model are listed in Table 3, as well as the model predictions for the age of the spikes.

Figure 6 displays the normalized stratigraphic heights of the ^{14}C samples and the paleointensity samples for each dataset. Boundaries of layers are displayed as horizontal lines (4 layers in KEN, and 10 layers in Timna-30). The distribution functions of the modeled ages are plotted according to their stratigraphic heights, and their medians are marked as open circles. We connected the medians of the two spikes in a straight line in order to obtain a simple linear age–height model for Timna-30 and stratum M3 in KEN. Since the upper stratum of KEN (i.e. M1/M2) is characterized by a different deposition rate (Levy et al., 2008), we applied a similar approach for M1/M2, connecting the medians of the earlier spike and the most upper ^{14}C sample in a straight line. The approach in this model is constructing a simple age–height model using the modeled ages of the spikes as endpoint markers.

3.5. A composite quasi-continuous absolute archaeointensity curve

The combined archaeointensity curve of Timna-30 and KEN is plotted as VADM versus age in Figure 7. A significant output of the combined model is that the two datasets agree remarkably with each other, even though they were constructed independently using different materials (type-A slag and type-B slag in Timna-30, and Mn-rich slag, a potsherd, and a furnace fragment in KEN). Only two samples show a difference from the general trend. 1) the early spike recorded in KEN shows a higher value than recorded in Timna-30.

Table 3
^{14}C ages and composite Bayesian modeled dates of Timna-30 and KEN[a].

Sample ID	Site	^{14}C age BP	Un-modeled calibrated date BCE (1σ)	Modeled date BCE (1σ)	Modeled date BCE (2σ)	Mean (median) modeled date BCE
17630[b]	KEN	2764±25[b]	969–846	886–846	902–832	866 (867)
12436[b]	KEN	2659±32[b]	834–799	896–866	906–836	876 (880)
Spike event				908–874	923–846	888 (890)
S2-w1	Timna-30	2705±35	895–816	917–886	937–862	902 (901)
S2-g1	Timna-30	2814±34	1006–921	949–909	981–899	935 (932)
S1-g1	Timna-30	2819±35	1011–921	980–926	1004–915	957 (955)
17641[b]	KEN	2767±25[b]	971–848	932–897	972–877	916 (915)
17643[b]	KEN	2813±26[b]	1001–927	973–920	998–911	950 (947)
17642[b]	KEN	2781±25[b]	976–898	969–902	992–891	932 (928)
Spike event				1012–941	1026–925	978 (980)
S1-d3	Timna-30	2893±39	1129–1008	1033–981	1066–936	1007 (1009)
S1-w7	Timna-30	2859±34	1111–946	1053–995	1105–941	1025 (1023)
17644[b]	KEN	2824±25[b]	1008–932	1026–976	1048–942	999 (1001)
17646[b]	KEN	2871±26[b]	1112–1005	1047–993	1086–938	1016 (1016)

[a] Calibrated and modeled using Oxcal 4.1.6 program (Ramsey, 2009; Reimer et al., 2009). The stratigraphic model is illustrated in Fig. S2, supplementary material, and in Fig. 6.
[b] ^{14}C age is from Levy et al. (2008).

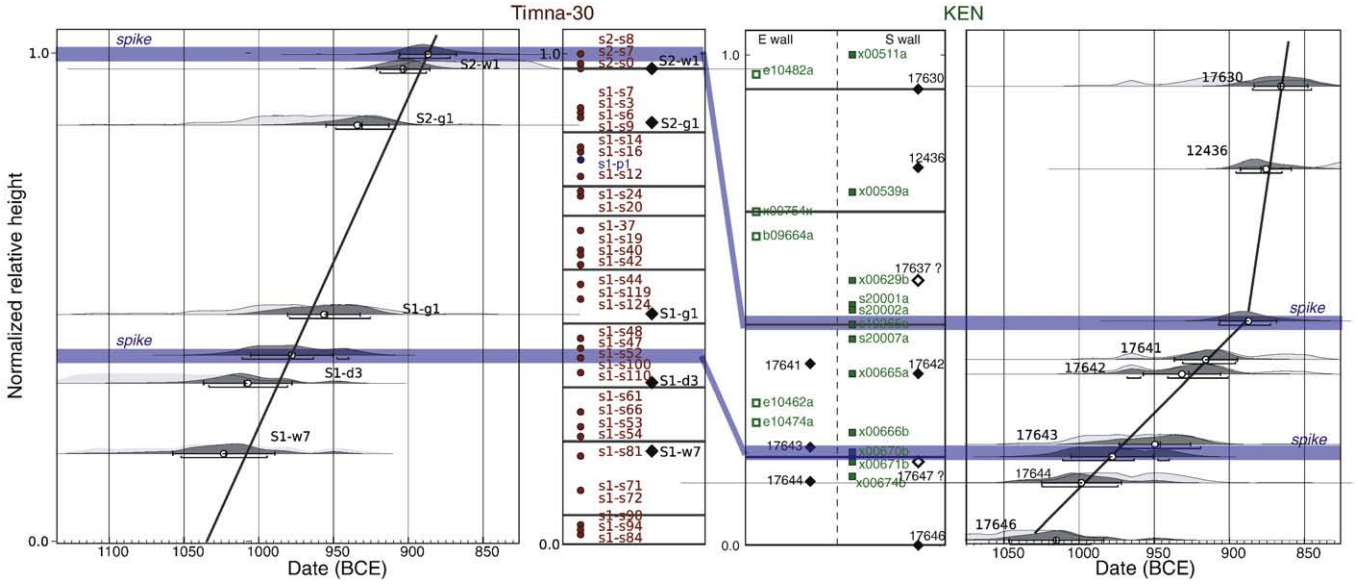

Fig. 6. Combined age-height model of KEN and Timna-30. Horizontal lines represent relative stratigraphic height of strata boundaries. Red circles represent stratigraphic location of slag samples in Timna-30. Green filled (open) squares represent location of paleointensity samples in KEN southern (eastern) cross-section. Distribution functions of the calibrated radiocarbon dates (Bayesian modeled dates) are colored in gray (black). Linear age–height model of each section is represented as a straight line connecting the medians of the distribution functions of the spikes events (pale blue horizontal lines), and the upper most sample in KEN.

This may be a result of the different material used (a furnace fragment versus slag), or due to the fact that the fast change in the intensity evident in the data (the peak of the spike may be as short as few years), was not captured by the slag analyzed in Timna-30. 2) Sample e10462a in KEN yields a low value with respect to the curve. Yet, it is hard to provide a possible source for this difference.

The large number of highly accurate paleointensity determinations, sequentially distributed over a short period of probably 200 years, enables a construction of a quasi-continuous archaeointensity curve of unprecedented resolution. Figure 7 displays the final curve, at a time-resolution of decades or better, and at an intensity resolution of 94%. This unique curve covers the growth and the decay of two dramatic geomagnetic spikes. The detailed characterization of these spikes places upper limits for two of the most fundamental properties of field behavior: amplitude and frequency of intensity variations. During the geomagnetic spike between 910 and 890 BCE, the field intensity changed rapidly from a VADM of 127 ± 4 ZAm^2 to 204 ± 12 ZAm^2 in about twenty years. Similar behavior is observed around 980 BCE when the VADM soared from 144 ± 3 ZAm^2 to 189 ± 3 ZAm^2 (possibly as high as 250 ZAm^2, as indicated in KEN) and then dropped again to 133 ± 7 ZAm^2 over an interval of less than twenty years. We therefore re-define here the maximum VADM variability as >70 ZAm^2 in a few decades and raise the maximum VADM value to at least 204 ± 12 ZAm^2.

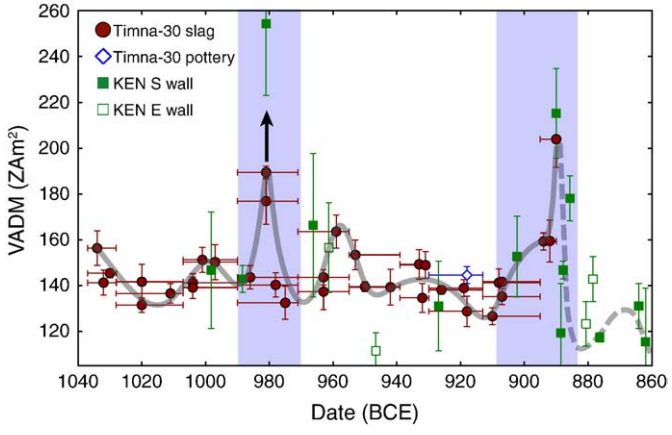

Fig. 7. VADM curve of the southern Levant from this work. Timna-30 slag (pottery) is marked as red circles (open diamond), KEN (Ben-Yosef et al., 2009) southern (eastern) wall are marked as filled (open) green squares. Vertical error-bars represent standard deviation of samples means. Horizontal error-bars in Timna-30 represent the layer boundaries. The solid curve is constructed by a weighted cubic-spline interpolation of the Timna-30 data points. The dashed curve is drawn by hand, illustrating our interpretation of field behavior after the 9th century spike. Pale blue areas show the two events of geomagnetic spikes. Arrow marks a high spike value in KEN not captured in Timna.

4. Discussion

This manuscript reports a study designed to recover short-term variations in the geomagnetic field intensity. The aim of the study is to construct a high-resolution archaeointensity curve of the Levant during a period, which has been recently evidenced with exceptionally high field values (Ben-Yosef et al., 2008a, 2009). This work is a direct continuation of Shaar et al. (2010) who established the platform for this study. Shaar et al. (2010) characterized the magneto-mineralogical properties of the slag found in Timna-30 and evaluated experimentally the accuracy and precision of paleointenisty derived from IZZI experiments on slag material. A discussion on the technical procedure of the paleointenisty methodology applied in this study can be found in Shaar et al. (2010). In the discussion below, we first examine the quality of the paleointensity data and the interpretation of the results, as well as the age model we use (Sections 4.1–4.3). Then, we conclude, on the basis on the results and the interpretation, that the geomagnetic field had experienced significant short-term variations, accompanied with high field fluctuations, namely "geomagnetic spikes" (Ben-Yosef et al., 2009), during the 10th and 9th centuries BCE. The implications of the new data for geomagnetism as well as for archaeology are discussed in Sections 4.4 and 4.5.

4.1. Interpretation of the paleointenisty experimental data

The paleointenisty procedure is, by definition, a routine designed to estimate the ancient field by an interpretation of experimental data. Thus,

subjective considerations are built into the paleointensity procedure, giving rise to a long discussion on the "proper" way to interpret paleointensity experiments (e.g. Selkin and Tauxe, 2000; Tauxe, 2010; Valet, 2003). In this work we tried to eliminate, to the extent possible, subjective considerations in interpreting the data, as pointed below.

One way to minimize the effect of subjective judgments in paleointensity interpretations is to determine a set of strict threshold values for paleointenisty statistics as selecting criteria (Table 1). The β parameter is lower than 0.055 ensuring that the best-fit line of the Arai plot is calculated using a quasi-linear segment with uncertainty in slope calculation caused by scattering lower than ~5%. The f_{vds} parameter is higher than 0.8 ensuring that the segment of the Arai plot includes more than 80% of the ancient TRM. Together, these parameters eliminate the possibility of the curved Arai plot with a large undefined uncertainty. In addition, the DRATS parameter ensures that no (or very little) alteration occurred during the experiments. The MAD and the DANG parameters are lower than 6°, ensuring stable TRM converging towards the origin in the orthogonal plots. All together, these threshold values allow for only a few options for choosing the interval for the calculation, minimizing subjective judgments in choosing the temperature bounds. Further control on the quality, at the sample level, is achieved by rejecting samples with standard deviation higher than 6%, or with less than 3 successful specimens. In summary, we argue that the values of the selecting criteria allow for maximum screening of specimens with linear Arai plots and orthogonal plots, ideal for reliable paleointenisty determinations. In practice, the statistics presented in Table S2, and in Figure S4, supplementary material, demonstrate paleointensity statistics that are much better than those determined by the threshold values.

Figure S4, supplementary material, shows that the slag material from site Timna-30 is characterized with an unusual high-quality behavior in the paleointenisty procedure. This behavior was not achieved by accident, but through a carefully developed sampling strategy in the field and in the laboratory, aiming at isolating only the glassy slag that demonstrated excellent behavior in the precursor study (Shaar et al., 2010). It is worth emphasizing a point raised by Ben-Yosef et al. (2008a,b) that slag material, in general, appears in various textures, sizes, and compositions. Thus, a careful sampling strategy is required for identifying the most suitable material.

Finally, the credibility of the results is significantly enhanced by the fact that the magnetic properties of the remanence carriers have been well characterized using samples from Timna-30 in Shaar et al. (2010). The remanence carriers in type-A slag were characterized as SD Mn–Fe oxides (jacobsite), and the remanence carriers in type-B slag were characterized as SD-PSD impure magnetite. In addition, the empirical test study of a re-melted slag (very similar to "type-B" slag) not only helped establishing a reliable experimental routine, but also showed that suitable samples lead to accurate paleointensity determination in high precision. Shaar et al. (2010) also concluded that uncertainties caused by cooling rate can be neglected in slag material, and that uncertainties caused by non-linear TRM effect can be minimized by using an oven field similar to the expected ancient field.

In summary, by applying the selection criteria listed in Table 2 on well-defined slag material, and by accepting the results and the conclusions of Shaar et al. (2010) we argue that accuracy is better than 94% and the precision is better than 6%, for all the samples analyzed in this study.

4.2. High field anomalies: statistical outlier or natural short-lived features (spikes)?

Assuming the selection criteria described in Section 4.1 yield data that accurately reflect changes in the geomagnetic field, an inspection of the results presented in Table 2 and Figure 5b leads to the following observations: 1) thirty-two data points are in the range between ~130 and ~160 ZAm^2, demonstrating paleointensity variations with wavelengths in the range of a few decades, and amplitudes in the range of 20–30 ZAm^2, and 2) three data points show extremely high values of 177–204 ZAm^2. One question regarding the interpretation of this dataset is: "are these high apparent geomagnetic fields short-lived geophysical features (i.e. geomagnetic spikes) or statistical outliers?"

An interpretation of the anomalies as outliers is plausible. However, interpreting the results as natural geophysical features is favored, because of the following reasons: 1) the dataset consists of high anomalies, but no low anomalies. As discussed in detail in Section 4.1, the technical quality of the data ensures high accuracy for all samples, and we cannot think of a convincible explanation why some samples would have a systematic error leading to high values (Arai plots of the samples with the highest field intensity are given in Figure S5, supplementary material, showing linear behavior). 2) Figure 5a illustrates high field anomalies in the KEN dataset, which is of the same age of the Timna-30 dataset. The Timna-30 dataset is therefore, an independent test for the hypothesis raised by Ben-Yosef et al. (2009) regarding the occurrence of geomagnetic spikes. Not only that the relative stratigraphical sequence confirms the occurrence of two independent spikes (Fig. 5), but also a composite VADM-age curve constructed by tying the two spikes to the same events (Fig. 6) demonstrates a remarkable agreement between the two datasets. 3) A geomagnetic spike is by definition a short event that is hard to detect, even with dense sampling. Therefore, we expect spikes to occur in only a few samples, yet in a tight stratigraphical position.

4.3. Age modeling of short-term features

Age modeling of short-term geomagnetic features is tricky for two reasons. First, the uncertainty of the calibrated ^{14}C age depends strongly on the ^{14}C calibration curve. Second, the calibration curve is flat and high during the period from the 11th to the 9th centuries BCE, leading to relatively large uncertainties in the calibrated ages. In this paper we adopt a Bayesian approach that helps substantially reduce the age uncertainties and find the best constrained model ages. Three assumptions were used in constructing the model. The first is the stratigraphic order of the samples in each dataset. The second is that the spikes in the two datasets are tied to the same events. The benefit in using these assumptions is in adding temporal constraints to the model. The third assumption is that the accumulation rate is reasonably constant, and we used the estimated dates of the spikes as end-points for calculating the accumulation rate in a simple straightforward way.

Figure S2 in the supplementary material tests the model, and presents two alternative age models for site Timna-30 and KEN, constructed by a Poisson-process accumulation model using the Oxcal program (Ramsey, 2009; Reimer et al., 2009). These alternative models allow for fluctuations in the accumulation rate, and therefore are suitable for the general case of non-uniform accumulation rate. The models do not include the boundaries of the layers, and they assume a continuous accumulation. A comparison of the two independent models of KEN and Timna-30 shows that the two datasets are partly of the same age, and that the $1-\sigma$ (63%) uncertainty associated with the high field anomalies (spikes) in both datasets coincide. These models therefore support our approach of tying the two datasets using the spikes events towards a composite age model. Of course, any other correlation would result in additional geomagnetic spikes (up to four) and more rapid field fluctuations, neither of which are demanded by the data. The correlation of the two spikes is therefore the most conservative interpretation of the data and is entirely consistent with independent age constraints provided by the radiocarbon dates.

4.4. Constraints for maximum amplitude and frequency of field behavior

Archaeomagnetic models and absolute paleointensity compilations of the past few thousands of years (e.g. Genevey et al., 2008; Korte and

Constable, 2005a,b; Yang et al., 2000) describe a peak in the geomagnetic field intensity in Eurasia around ~2700–3000 BP, very close to the time of the local Levantine geomagnetic spikes. A global VADM compilation of the past 50,000 years (Knudsen et al., 2008) implies that this geomagnetic peak was the highest in the late Quaternary (Fig. 1a). An independent indication for a globally strong geomagnetic field during the Levantine Iron Age is the paleointensity reconstruction curve based on cosmogenic nuclides, which predicts that the highest geomagnetic peak in the past 40,000 years was at ~2700 BP (Muscheler et al., 2005). Absolute paleointensities prior to 50 kya are sparser, but they show, in general, lower field intensities than during the Iron Age (Tauxe, 2006; Tauxe and Yamazaki, 2007). The Iron Age may, therefore, be a unique period in the perspective of geomagnetic field evolution, as it possibly marks a significant global peak in the strength of the geomagnetic field.

Recent secular variation models based on spherical harmonics (Korte and Constable, 2005a; Korte et al., 2009) predict high geomagnetic field strengths over Europe and the Near East at ~3000 BP. They predict that despite the strong field over Eurasia, the total strength of the geomagnetic dipole did not experience significant variations during the Iron Age. The large number of archaeointensity determinations from Europe may, therefore, bias the global VADM stack (Knudsen et al., 2008) towards higher values at ~3000 BP. According to this interpretation, the high field in the Levant, showing an average of 160 ZAm^2 at ~3000 BP, could be the part of a large high field lobe that extended towards Europe.

Regardless of whether the spikes are global (dipole source) or local (higher order multipole), the importance of our finding is the extreme high amplitude and short wavelength of field behavior. The Levantine local geomagnetic peak shows an averaged VADM of ~160 ZAm^2, and spikes in excess of 200 ZAm^2. Thus, the new curve describes one of the most dramatic episodes in the geomagnetic record, featuring some of the highest field intensities ever recorded. The resolution and the accuracy of the new curve help place firm limits for the maximum strength of the field, as well as for its rate of change. These fundamental properties should be considered in any future modeling of the geomagnetic secular variations.

4.5. Geodynamo mechanisms

The current quasi-continuous absolute paleointensity curve allows for a time-resolution that is beyond the capability of most conventional paleomagnetic methodologies. Only records constructed by direct instrumental measurements can provide similar resolution, but they span historically only over the past 150 years for intensity, and over the past 400 years for direction. The high-resolution historical data allowed researchers to discern dynamical changes in the geodynamo through numerical simulations of the geodynamo (NGD). NGD models have successfully drawn the behavior of local short-lived flux patches that grow and disappear over timescales ranging from decades to centuries (e.g. Gubbins et al., 2006; Jackson et al., 2000). Modern satellite measurements have extended the resolution of NGD models, and they have revealed short-term changes on timescales of the order of decades, such as equatorial flux spots (Jackson, 2003), and even on timescales in the order of months, such as local accelerations of fluid flow (Olsen and Mandea, 2008). The expression of all these known short-lived geodynamo features on Earth's surface, in terms of VADM variability, is much lower than the Levantine spikes. Therefore, a geodynamo mechanism that could generate the extremely rapid variations we observe during the Iron Age is yet to be found.

Geodynamo features inferred from NGD models are all associated with a weakening geomagnetic dipole (Olson and Amit, 2006) and reverse polarity patches that are driving the decrease in moment of the geomagnetic dipole (Gubbins, et al., 2006; Olson and Amit, 2006). However, the Iron Age is different as it is characterized by a rapidly growing geomagnetic dipole. The geomagnetic spikes may be, therefore, a product of a highly active normal polarity flux patch that works to increase the dipole moment. The instability and the short duration of the spikes can be caused by mechanisms such as magnetic upwelling (Bloxham, 1986; Gubbins, 2007) or plumes (Aubert et al., 2008). Alternatively, short-lived fluctuations may indicate a possible existence of "magnetic storms" in the core. Yet, a better spatial resolution and directional paleomagnetic data are needed to test any hypothesis regarding possible geodynamo mechanisms.

4.6. Implications for archaeological sciences

A detailed description of the geomagnetic secular variations can provide a useful and independent dating tool in archaeological science (e.g. Lanos et al., 2005; Le Goff et al., 2002). Ben-Yosef et al. (2010) recently applied the archeointensity curve of the Levant to constrain the age of an Iron Age copper-smelting site. A similar approach can be used, in general, in cases where ^{14}C or ceramic typology cannot resolve dates. Yet, the resolution and the robustness of archaeomagnetic dating techniques depend on the quality of the secular variation curve being used for the region. Therefore, it is essential to expand the archaeomagnetic data of the Levant, and include a large number of well-dated paleointensity estimates as well as paleomagnetic directions in it.

This study demonstrates a unique application of paleomagnetism in archaeology (archaeomagnetism). The well-dated sites of KEN and Timna-30 are correlated using their paleointensity behavior. We show that the paleomagnetic correlation constrains the ^{14}C modeled ages and refines their chronology (Figs. 6 and 7). The resulting high-resolution archaeointensity curve may be useful in future studies, providing a reference curve for dating other archaeological contexts of the same age. In the Levant, the new archaeointensity curve for the 10th and 9th century BCE coincides with the Biblical period, in which correlations between archaeological sites, biblical accounts and rapid historical events are hotly debated (e.g. Levy and Higham, 2005). We therefore suggest using the presented curve as an additional correlation tool for biblical sites.

5. Conclusions

1. Maximum intensity of the geomagnetic field, in terms of local VADM, can reach at least 204 ± 12 ZAm^2, as inferred from highly accurate paleointenisty estimates based on slag material with SD properties.
2. Maximum temporal variability of geomagnetic field intensity can be as high as 70 ZAm^2 or higher over periods that are shorter than few decades.
3. Archaeointensity estimates from two different locations, using different source materials, demonstrate excellent agreement, enhancing the robustness of the IZZI absolute paleointensity methodology (Tauxe, 2010), when applied to suitable samples.
4. We present a high-resolution ^{14}C based archaeointensity curve of the Levant from the late 11th century to the 9th century BCE that offers the possibility for archaeological tool for dating as well as for correlation.
5. Further study of the spike episodes and the global paleointensity peak should include additional paleomagnetic sites elsewhere, as well as directional paleomagnetic analyses, in order to test whether they were local features or geomagnetic dipole phenomenon.

Acknowledgments

The authors wish to thank the management and staff of the Timna Park and the Israeli Antiquities Authority for their support of the excavation (license #G-38/2009 to E.B.-Y.). We thank Jason Steindorf

for helping with the measurements, and also to Hai Ashkenazi and Uri Davidovich for their help in the field. We thank Y. Ritov and C. Constable for fruitful discussions. We thank Joshua Feinberg and Yehoshua Kolodny for comments and suggestions that substantially improved the manuscript. We thank Yehuda Enzel for his assistance and useful discussion. The manuscript was greatly improved by the constructive comments of the editor P. DeMenocal and by the comments of Andrew Biggin and an anonymous reviewer. This work was partially funded by the US–Israel Binational Science Foundation grant 85739A (H.R. and L.T.), and NSF grants EAR0636051 and EAR0944137 to LT.

Appendix A. Supplementary data

Supplementary data to this article can be found online at doi:10.1016/j.epsl.2010.11.013.

References

Aubert, J., Aurnou, J., Wicht, J., 2008. The magnetic structure of convection-driven numerical dynamos. Geophys. J. Int. 172, 945–956.
Ben-Yosef, E., Tauxe, L., Ron, H., Agnon, A., Avner, U., Najjar, M., Levy, T.E., 2008a. A new approach for geomagnetic archaeointensity research: insights on ancient metallurgy in the southern Levant. J. Archaeol. Sci. 35, 2863–2879.
Ben-Yosef, E., Ron, H., Tauxe, L., Agnon, A., Genevey, A., Levy, T.E., Avner, U., Najjar, M., Ben-Yosef, E., Ron, H., Tauxe, L., Agnon, A., Genevey, A., Levy, T.E., Avner, U., Najjar, M., 2008b. Application of copper slag in geomagnetic archaeointensity research. J. Geophys. Res.-Sol. Earth 113.
Ben-Yosef, E., Tauxe, L., Levy, T.E., Shaar, R., Ron, H., Najjar, M., 2009. Geomagnetic intensity spike recorded in high resolution slag deposit in southern Jordan. Earth Planet. Sci. Lett. 287, 529–539.
Ben-Yosef, E., Tauxe, L., Levy, T.E., 2010. Archaeomagnetic dating of copper smelting site F2 in the Timna valley (Israel) and its implications for the modelling of ancient technological developments. Archaeometry 52, 1110–1121.
Biggin, A.J., Thomas, D.N., 2003. The application of acceptance criteria to results of thellier palaeointensity experiments performed on samples with pseudo-single-domain-like characteristics. Phys. Earth Planet. Int. 138, 279–287.
Bloxham, J., 1986. The expulsion of magnetic-flux from the Earth's core. Geophys. J. R. Astron. Soc. 87, 669–678.
Coe, R.S., Gromme, S., Mankinen, E.A., 1978. Geomagnetic paleointensities from radiocarbon-dated lava flows on Hawaii and question of pacific nondipole low. J. Geophys. Res. 83, 1740–1756.
Donadini, F., Riisager, P., Korhonen, K., Kahma, K., Pesonen, L., Snowball, I., 2007. Holocene geomagnetic paleointensities: a blind test of absolute paleointensity techniques and materials. Phys. Earth Planet. Int. 161, 19–35.
Gallet, Y., Genevey, A., Courtillot, V., 2003. On the possible occurrence of 'archaeomagnetic jerks' in the geomagnetic field over the past three millennia. Earth Planet. Sci. Lett. 214, 237–242.
Genevey, A., Gallet, Y., 2002. Intensity of the geomagnetic field in Western Europe over the past 2000 years: new data from ancient french pottery. J. Geophys. Res.-Sol. Earth 107.
Genevey, A., Gallet, Y., Constable, C.G., Korte, M., Hulot, G., 2008. Archeoint: an upgraded compilation of geomagnetic field intensity data for the past ten millennia and its application to the recovery of the past dipole moment. Geochem. Geophys. Geosyst. 9.
Gubbins, D., 2007. Geomagnetic constraints on stratification at the top of Earth's core. Earth Planet. Space 59, 661–664.
Gubbins, D., Jones, A.L., Finlay, C.C., 2006. Fall in earth's magnetic field is erratic. Science 312, 900–902.
Jackson, A., 2003. Intense equatorial flux spots on the surface of the Earth's core. Nature 424, 760–763.
Jackson, A., Jonkers, A.R.T., Walker, M.R., 2000. Four centuries of geomagnetic secular variation from historical records. Philos. Trans. R. Soc. A 358, 957–990.
Kirschvink, J.L., 1980. The least-squares line and plane and the analysis of paleomagnetic data. Geophys. J. R. Astron. Soc. 62, 699–718.
Knudsen, M.F., Riisager, P., Donadini, F., Snowball, I., Muscheler, R., Korhonen, K., Pesonen, L.J., 2008. Variations in the geomagnetic dipole moment during the Holocene and the past 50 kyr. Earth Planet. Sci. Lett. 272, 319–329.
Korhonen, K., Donadini, F., Riisager, P., Pesonen, L.J., 2008. GEOMAGIA50: an archeointensity database with PHP and MySQL. Geochem. Geophys. Geosyst. 9.
Korte, M., Constable, C.G., 2003. Continuous global geomagnetic field models for the past 3000 years. Phys. Earth Planet. Int. 140, 73–89.
Korte, M., Constable, C.G., 2005a. Continuous geomagnetic field models for the past 7 millennia: 2. CALS7K. Geochem. Geophys. Geosyst. 6.
Korte, M., Constable, C.G., 2005b. The geomagnetic dipole moment over the last 7000 years — new results from a global model. Earth Planet. Sci. Lett. 236, 348–358.
Korte, M., Donadini, F., Constable, C.G., 2009. Geomagnetic field for 0–3 ka: 2. A new series of time-varying global models. Geochem. Geophys. Geosyst. 10.
Lanos, P., Le Goff, M., Kovacheva, M., Schnepp, E., 2005. Hierarchical modelling of archaeomagnetic data and curve estimation by moving average technique. Geophys. J. Int. 160, 440–476.
Le Goff, M., Gallet, Y., Genevey, A., Warme, N., 2002. On archeomagnetic secular variation curves and archeomagnetic dating. Phys. Earth Planet. Int. 134, 203–211.
Levy, T.E., Higham, T. (Eds.), 2005. The Bible and Radiocarbon Dating. Archaeology, Text and Science. Equinox, London. 448 pp.
Levy, T.E., Higham, T., Ramsey, C.B., Smith, N.G., Ben-Yosef, E., Robinson, M., Munger, S., Knabb, K., Schulze, J.P., Najjar, M., Tauxe, L., 2008. High-precision radiocarbon dating and historical biblical archaeology in southern Jordan. Proc. Natl. Acad. Sci. U.S.A. 105, 16460–16465.
Muscheler, R., Beer, R., Kubik, P.W., Synal, H.A., 2005. Geomagnetic field intensity during the last 60, 000 years based on Be-10 and Cl-36 from the Summit ice cores and C-14. Quatern. Sci. Rev. 24, 1849–1860.
Nagata, T., Arai, Y., Momose, K., 1963. Secular variation of the geomagnetic total force during the last 5000 years. J. Geophys. Res. 68, 5277–5282.
Olsen, N., Mandea, M., 2008. Rapidly changing flows in the Earth's core. Nat. Geosci. 1, 390–394.
Olson, P., Amit, H., 2006. Changes in Earth's dipole. Naturwissenschaften 93, 519–542.
Ramsey, C.B., 2009. Bayesian analysis of radiocarbon dates. Radiocarbon 51, 337–360.
Reimer, P.J., Baillie, M.G.L., Bard, E., Bayliss, A., Beck, J.W., Blackwell, P.G., Ramsey, C.B., Buck, C.E., Burr, G.S., Edwards, R.L., Friedrich, M., Grootes, P.M., Guilderson, T.P., Hajdas, I., Heaton, T.J., Hogg, A.G., Hughen, K.A., Kaiser, K.F., Kromer, B., McCormac, F.G., Manning, S.W., Reimer, R.W., Richards, D.A., Southon, J.R., Talamo, S., Turney, C.S.M., van der Plicht, J., Weyhenmeye, C.E., 2009. Intcal09 and Marine09 radiocarbon age calibration curves, 0–50, 000 years cal bp. Radiocarbon 51, 1111–1150.
Rothenberg, B., 1980. Die archaeologie des verhüttungslagers site 30. In: Conrad, H.G., Rothenberg, B. (Eds.), Antikes kupfer im timna-tal. Der Anschnitt, Bochum, pp. 187–213.
Selkin, P.A., Tauxe, L., 2000. Long-term variations in palaeointensity. Philos. Trans. R. Soc. A 358, 1065–1088.
Selkin, P.A., Gee, J.S., Tauxe, L., 2007. Nonlinear thermoremanence acquisition and implications for paleointensity data. Earth Planet. Sci. Lett. 256, 81–89.
Shaar, R., Ron, H., Tauxe, L., Kessel, R., Agnon, A., Ben-Yosef, E., Feinberg, J.M., 2010. Testing the accuracy of absolute intensity estimates of the ancient geomagnetic field using copper slag material. Earth Planet. Sci. Lett. 290, 201–213.
Tauxe, L., 2006. Long-term trends in paleointensity: the contribution of DSDP/ODP submarine basaltic glass collections. Phys. Earth Planet. Int. 156, 223–241.
Tauxe, L., 2010. Essentials of Paleomagnetism. University of California Press.
Tauxe, L., Staudigel, H., 2004. Strength of the geomagnetic field in the Cretaceous normal superchron: new data from submarine basaltic glass of the Troodos ophiolite. Geochem. Geophys. Geosyst. 5.
Tauxe, L., Yamazaki, T., 2007. Paleointensities. In: Kono, M. (Ed.), Geomagnetism, Treatise on Geophysics, 5. Elsevier, pp. 509–563.
Valet, J.P., 2003. Time variations in geomagnetic intensity. Rev. Geophys. 41.
Yang, S., Odah, H., Shaw, J., 2000. Variations in the geomagnetic dipole moment over the last 12 000 years. Geophys. J. Int. 140, 158–162.